

Research Article

A Sliding Mode Control with Nonlinear Fractional Order PID Sliding Surface for the Speed Operation of Surface-Mounted PMSM Drives Based on an Extended State Observer

Peng Gao ^{1,2}, Guangming Zhang ¹, Huimin Ouyang ¹, and Lei Mei¹

¹College of Electrical Engineering and Control Science, Nanjing Tech University, Nanjing 211899, China

²College of Electrical Engineering, Tongling University, Tongling 244000, China

Correspondence should be addressed to Guangming Zhang; zgm@njtech.edu.cn

Received 27 May 2019; Revised 30 July 2019; Accepted 17 August 2019; Published 18 September 2019

Academic Editor: Sajad Azizi

Copyright © 2019 Peng Gao et al. This is an open access article distributed under the Creative Commons Attribution License, which permits unrestricted use, distribution, and reproduction in any medium, provided the original work is properly cited.

A novel sliding mode controller (SMC) with nonlinear fractional order PID sliding surface based on a novel extended state observer for the speed operation of a surface-mounted permanent magnet synchronous motor (SPMSM) is proposed in this paper. First, a new smooth and derivable nonlinear function with improved continuity and derivative is designed to replace the traditional nonderivable nonlinear function of the nonlinear state error feedback control law. Then, a nonlinear fractional order PID sliding mode controller is proposed on the basis of the fractional order PID sliding surface with the combination of the novel nonlinear state error feedback control law to improve dynamic performance, static performance, and robustness of the system. Furthermore, a novel extended state observer is designed based on the new nonlinear function to achieve dynamic feedback compensation for external disturbances. Stability of the system is proved based on the Lyapunov stability theorem. The corresponding comparative simulation results demonstrate that the proposed composite control algorithm displays good stability, dynamic properties, and strong robustness against external disturbances.

1. Introduction

Permanent magnet synchronous motor (PMSM) gradually becomes one of the most competitive motion control products because of the inherent advantages of low rotor inertia, high efficiency, and high power density, which has been utilized in industrial applications [1–3]. In such applications, the speed control for PMSMs becomes a critical task. Because the traditional PID has the advantages of simple structure and being easy to implement, the traditional PID controller is still widely used in the control of PMSMs [4]. However, because of the nonlinear, time-varying, strong coupling of PMSMs, it is difficult to achieve satisfactory motor performance by the use of the traditional PID control algorithm [5]. Therefore, various advanced nonlinear controllers have been applied for the control of PMSMs, such as the backstepping controller [6, 7], predictive controller [8, 9], active disturbance rejection controller [10, 11], fuzzy logic controller [12], and neural network controller [13].

In recent years, the SMC has become one of the most used nonlinear control methods. Due to the fact that the SMC has many advantages, such as fast response, robustness to parameter variations and external disturbances, and simple realization, it has become a hot topic in the field of nonlinear control [14–17]. Many improved SMC strategies were also widely used for the control of PMSMs. In Wang et al.'s paper [18], an adaptive SMC based on an improved sliding mode reaching law was introduced for the control of PMSMs. In another research [19], a nonsingular terminal SMC was proposed for the speed control of PMSMs. A novel speed controller was designed by the nonsingular terminal SMC with a disturbance observer for the velocity control of PMSMs [20]. In some researches [21, 22], an adaptive SMC was designed for the speed and current control of PMSMs. In another research [23], a new exponential reaching law of the SMC strategy was proposed to improve the performance of the control of PMSMs. Fractional order calculus has been widely used for the

improvement of the SMC. Traditional integer order calculus can be broadened by using the fractional order calculus to be arbitrary numbers. Researchers have designed many SMC strategies by using fractional order calculus. For example, a fractional order SMC algorithm was designed for the control of antilock braking systems [24]. In another research [25], a fractional order SMC strategy based on parameter autotuning was designed for the velocity control of PMSMs. A fractional order exponential switching technique was designed to enhance the SMC strategy in [26]. In Yang et al.'s paper [27], a fractional order terminal SMC algorithm was designed for the control of the buck converter. In Kerrouche et al.'s paper [28], a fractional order SMC strategy was designed for the control of the distribution static synchronous compensator. An adaptive supertwisting fractional order nonsingular terminal SMC strategy was designed for the control of cable driven manipulators in [29]. The fractional order PID (FOPID) sliding mode variable structure controller (SMC-FOPID) was designed by utilizing the FOPID sliding surface in references [30–33]. An extended state observer (ESO) and a nonlinear state error feedback control law (NLSEF) were proposed by Han [34]. The NLSEF was adopted to confine errors in the systems, and the ESO was widely utilized to estimate the unknown disturbances of nonlinear systems [35–37].

In order to improve that dynamic performance, static performance, and robustness of the SMC-FOPID and considering the advantages of the NLSEF, a novel nonlinear FOPID (NFOPID) sliding surface is developed in this study. First, a new continuous and derivable nonlinear function with improved continuity and derivative is designed to replace the traditional nonderivable nonlinear function of the traditional NLSEF; then, based on the FOPID and with the combination of a novel NLSEF, a novel NFOPID sliding surface is developed; lastly, an improved SMC with the novel NFOPID sliding surface (SMC-NFOPID) is proposed for the speed control of the SPMSM in this work. Because of the inclusion of the novel NLSEF, the controller can improve dynamic performance, static performance, and robustness of the system. To the best of our knowledge, the structure of the SMC-NFOPID strategy is first proposed in the existing literature. Furthermore, a novel ESO based on the new nonlinear function is designed combining the SMC-NFOPID strategy in order to eliminate the influences caused by sudden load fluctuations in this paper.

This paper is organized as follows: A typical mathematical model of the SPMSM is introduced in Section 2. A novel NLSEF is designed on the basis of a new continuous and derivable nonlinear function, a novel NFOPID sliding surface is proposed based on the FOPID with the combination of the novel NLSEF, and an SMC-NFOPID strategy based on a novel ESO is designed for the speed control of the SPMSM in Section 3. Stability of the system is proved on the basis of the Lyapunov stability theorem in Section 4. Comparative simulations and analysis are illustrated in Section 5. Finally, some conclusions are given in Section 6.

2. Mathematical Model of the SPMSM

PMSM is a nonlinear, strong-coupled, and multivariable complex system. A common dq -axis mathematical model is used to analyze the PMSM in this section.

The flux linkage equation of the PMSM in the synchronous rotating reference frame is as follows:

$$\begin{cases} \varphi_d = L_d i_d + \varphi_f, \\ \varphi_q = L_q i_q, \end{cases} \quad (1)$$

where φ_f is the flux linkage of the permanent magnet; φ_d and φ_q are the d - and q -axis flux linkages, respectively; L_d and L_q are the d - and q -axis inductances, respectively; and i_d and i_q are the stator currents of the d - and q -axis, respectively.

The voltage equation of the PMSM in the synchronous rotating reference frame is as follows:

$$\begin{cases} u_d = R i_d + \dot{\varphi}_d - \omega \varphi_q, \\ u_q = R i_q + \dot{\varphi}_q + \omega \varphi_d, \end{cases} \quad (2)$$

where R is the stator resistance; u_d and u_q are the d - and q -axis stator voltages, respectively; and ω is the mechanical rotor angular speed of the PMSM.

Electromagnetic torque equation is as follows:

$$T_e = p_n (\varphi_d i_q - \varphi_q i_d), \quad (3)$$

where T_e is the electromagnetic torque and p_n is the number of pole pairs; substituting (1) into (3), we get

$$T_e = p_n (\varphi_f i_q + (L_d - L_q) i_d i_q). \quad (4)$$

The SPMSM is considered, and we have $L_d = L_q = L$; then, (4) can be rewritten as follows:

$$T_e = p_n \varphi_f i_q. \quad (5)$$

Under a mechanical load torque, the mechanical equation of the SPMSM can be expressed as follows:

$$T_e - T_L = \frac{J}{p_n} \dot{\omega} + B\omega, \quad (6)$$

where J is the rotational inertia, B is the viscous friction coefficient, and T_L is the applied external load torque.

Afterwards, with the control strategy of $i_d = 0$, the state equation of the SPMSM can be obtained as follows:

$$\dot{i}_q = \frac{1}{L} u_q - \frac{R}{L} i_q - \frac{p_n \varphi_f}{L} \omega, \quad (7)$$

$$\dot{\omega} = \frac{3p_n \varphi_f}{2J} i_q - \frac{B}{J} \omega - \frac{1}{J} T_L. \quad (8)$$

In order to achieve good stability, dynamic properties, and strong robustness against external disturbances, an SMC-NFOPID strategy with a novel ESO is designed for the speed control of SPMSM drive systems in this paper.

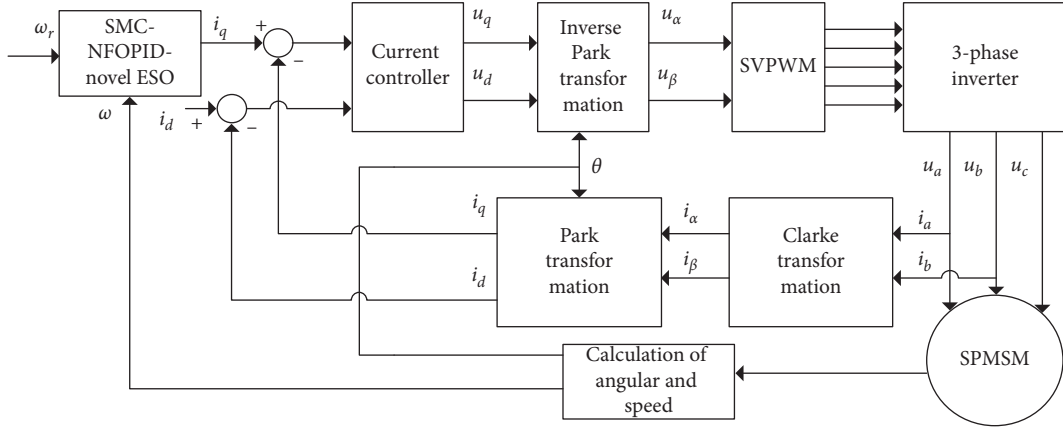


FIGURE 1: Configuration of the field-oriented control SPMSM servo drive.

3. Controller Design

The motor speed error is defined as

$$e(t) = \omega_r(t) - \omega(t), \quad (9)$$

where $e(t)$ is the tracking error, $e(t) \in R$; $\omega(t)$ is the mechanical rotor angular speed; and $\omega_r(t)$ is the given value of the mechanical rotor angular speed. Based on the SPMSM state equation, the speed control algorithm should guarantee the precise tracking of the reference angular speed value $\omega_r(t)$ of the motor.

The proposed sliding mode control with the NFOPID sliding surface for the speed operation of the SPMSM based on a novel ESO control structure diagram using the $i_d = 0$ control strategy is shown in Figure 1.

Definition 1 (referring to [23, 38]). The traditional sliding surface s can be defined as follows:

$$s(t) = ce(t) + \dot{e}(t), \quad (10)$$

where c is the positive coefficient.

In the meantime, to further ensure high performance in the reaching phase, we choose the following exponential reaching law:

$$\dot{s}(t) = -ks(t) - \eta \text{sign}(s(t)), \quad (11)$$

where $k \in R^+$ and $\eta \in R^+$ are the switching gain and exponential coefficient of the regular exponential reaching law, respectively, and $\text{sign}(s)$ is the sign function, which is defined as follows:

$$\text{sign}(s) = \begin{cases} 1, & s > 0, \\ 0, & s = 0, \\ -1, & s < 0. \end{cases} \quad (12)$$

Taking the time derivative of the sliding mode surface (10) and substituting (10) into (11), we obtain

$$c\dot{e}(t) - \ddot{e}(t) = -ks(t) - \eta \text{sign}(s(t)). \quad (13)$$

Sequentially, substituting (8) and (9) into (13), we get

$$c\dot{e}(t) - \frac{3p_n\phi_f}{2J}i_q = -ks(t) - \eta \text{sign}(s(t)). \quad (14)$$

Therefore, the control law of the traditional SMC (TSMC) is designed as follows:

$$i_q = \frac{2J}{3p_n\phi_f} \int_0^t [c\dot{e} + ks(t) + \eta \text{sign}(s(t))] d\tau. \quad (15)$$

The generalization of integration and differentiation to noninteger order is fractional calculus [32].

Definition 2 (referring to [32, 33]). In the fractional calculus, $\Gamma(\cdot)$ is the gamma function given by

$$\Gamma(z) = \int_0^\infty e^{-\gamma} \gamma^{z-1} d\gamma, \quad (16)$$

which satisfies $R(z) > 0$.

Definition 3 (referring to [32, 33]). The α th-order Riemann–Liouville fractional derivative of function $f(t)$ with respect to t and the terminal value t_0 is given by

$${}_{t_0}D_t^\varepsilon f(t) = \frac{1}{\Gamma(1-\varepsilon)} \frac{d}{dt} \int_{t_0}^t \frac{f(\tau)}{(t-\tau)^\varepsilon} d\tau, \quad (17)$$

where $0 < \varepsilon < 1$.

The Riemann–Liouville definition of the α th-order fractional integration is given by

$${}_{t_0}D_t^u f(t) = \frac{1}{\Gamma(u)} \frac{d}{dt} \int_{t_0}^t \frac{f(\tau)}{(t-\tau)^{1-u}} d\tau, \quad (18)$$

where $-1 < u < 0$.

Lemma 1 (referring to [31]). Fractional derivatives and integrals have the composition rules as follows:

$$\frac{d^n}{dt^n} ({}_{t_0}D_t^\varepsilon f(t)) = {}_{t_0}D_t^{\varepsilon+n} f(t), \quad (19)$$

$$\frac{d^n}{dt^n} ({}_{t_0}D_t^u f(t)) = {}_{t_0}D_t^{u+n} f(t).$$

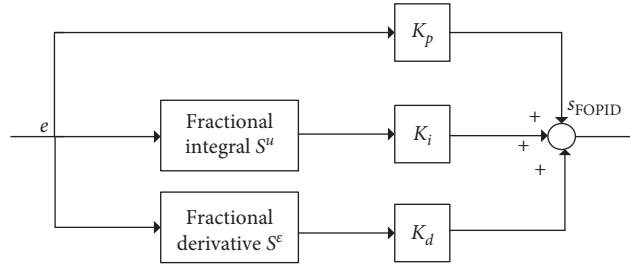
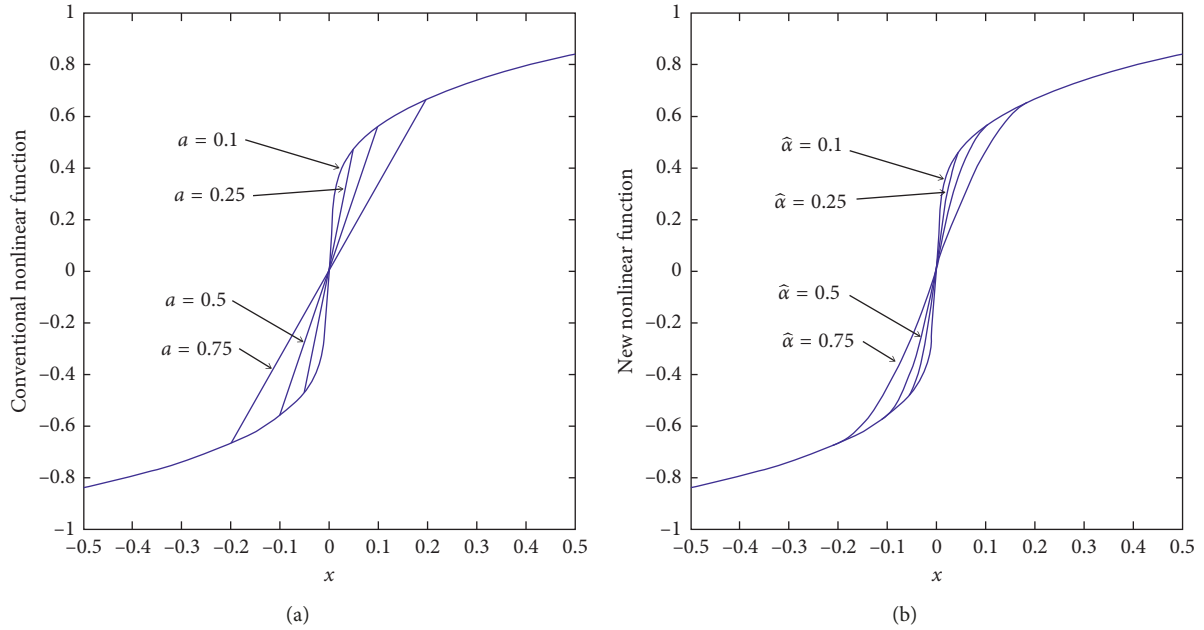


FIGURE 2: Block diagram of the FOPID sliding surface structure.

FIGURE 3: (a) Characteristic curves of $\text{fal}(\cdot)$, $\delta = 0.1$, $a = 0.1, 0.25, 0.5$, and 0.75 . (b) Characteristic curves of $f_{\text{new}}(\cdot)$, $\hat{\delta} = 0.1$, $\hat{\alpha} = 0.1, 0.25, 0.5$, and 0.75 .

Definition 4 (referring to [30–32]). The fractional order sliding PID surface s_{FOPID} can be defined as follows:

$$s_{\text{FOPID}}(t) = K_p e(t) + K_i D_t^u(e(t)) + K_d D_t^\epsilon(e(t)), \quad (20)$$

where K_p , K_i , and K_d are the positive coefficients.

The FOPID sliding surface structure diagram is shown in Figure 2.

An exponential reaching law is designed as follows:

$$\dot{s}_{\text{FOPID}}(t) = -k s_{\text{FOPID}}(t) - \eta \text{sign}(s_{\text{FOPID}}(t)). \quad (21)$$

Taking the time derivative of the sliding mode surface (20), according to Lemma 1, and substituting (20) into (21), (21) can be rewritten as follows:

$$K_p \dot{e}(t) + K_i D_t^{1+u}(e(t)) + K_d D_t^{\epsilon+1}(e(t)) = -k s_{\text{FOPID}}(t) - \eta \text{sign}(s_{\text{FOPID}}(t)). \quad (22)$$

Sequentially, substituting (8) and (9) into (22), equation (22) can be rewritten as

$$K_p \left(\dot{\omega}_r(t) - \frac{3p_n \varphi_f}{2J} i_q + \frac{T_L}{J} + \frac{B}{J} \omega(t) \right) + K_i D_t^{1+u}(e(t)) + K_d D_t^{1+\epsilon}(e(t)) = -k s_{\text{FOPID}}(t) - \eta \text{sign}(s_{\text{FOPID}}(t)). \quad (23)$$

Then, the control law of the SMC-FOPID can be designed as follows:

$$i_q = \frac{2J}{3p_n \varphi_f K_p} \left(\left(K_p \left(\dot{\omega}_r(t) + \frac{T_L}{J} + \frac{B}{J} \omega_r(t) \right) \right) + K_p \left(k - \frac{B}{J} \right) e(t) + K_i D_t^{1+u} e(t) + K_d D_t^{1+\epsilon} e(t) + k K_i D_t^u e(t) + k K_d D_t^\epsilon e(t) + \eta \text{sign}(s_{\text{FOPID}}(t)) \right). \quad (24)$$

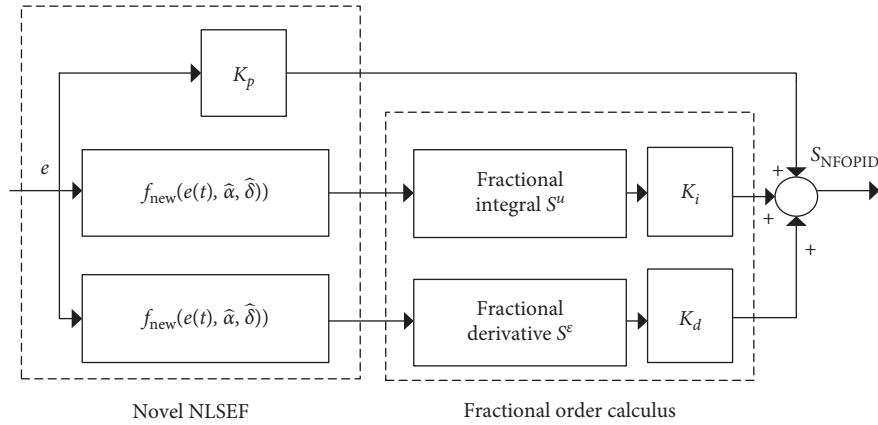


FIGURE 4: Block diagram of the proposed NFOPID sliding surface structure.

In order to improve the dynamic performance, static performance, and robustness of the FOPID-SMC, a novel NFOPID sliding surface is developed in this paper. The novel NFOPID sliding surface is based on FOPID by the combination of a novel NLSEF.

The core of the conventional NLSEF is the nonlinear function $\text{fal}(\cdot)$. The expression of the conventional nonlinear function $\text{fal}(\cdot)$ is given as follows [34]:

$$\text{fal}(x, \alpha, \delta) = \begin{cases} |x|^\alpha \text{sign}(x), & |x| > \delta, \\ \frac{x}{\delta^{1-\alpha}}, & |x| \leq \delta, \end{cases} \quad (25)$$

where δ and α are the filter factors and nonlinear factors of $\text{fal}(\cdot)$, respectively. The corresponding function curves of the function $\text{fal}(\cdot)$ are shown in Figure 3(a).

The nonlinear function $\text{fal}(\cdot)$ is continuous, but it is nonderivable, so the high-frequency flutter phenomenon will be produced by the function $\text{fal}(\cdot)$. Thus, a new nonlinear function $f_{\text{new}}(\cdot)$ is designed in this section. The function $f_{\text{new}}(\cdot)$ is a continuous and derivable nonlinear function, and it is expressed as follows:

$$f_{\text{new}}(x, \hat{\alpha}, \hat{\delta}) = \begin{cases} |x|^{\hat{\alpha}} \text{sign}(x), & |x| > \hat{\delta}, \\ \mathfrak{R}_1 x + \mathfrak{R}_2 x^2 + \mathfrak{R}_3 \text{ver sin}(|x|) \text{sign}(x), & |x| \leq \hat{\delta}, \\ \text{ver sin}(|x|) = 1 - \cos(|x|), \end{cases} \quad (26)$$

where $0 < \hat{\delta} < 1$, $0 < \hat{\alpha} < 1$, and $\mathfrak{R}_1, \mathfrak{R}_2, \mathfrak{R}_3$ are the parameters that need to be determined. Continuous and derivable conditions can be satisfied by the following expressions:

$$\begin{cases} f_{\text{new}}(x, \hat{\alpha}, \hat{\delta}) = \hat{\delta}^{\hat{\alpha}}, & e = \hat{\delta}, \\ f_{\text{new}}(x, \hat{\alpha}, \hat{\delta}) = -\hat{\delta}^{\hat{\alpha}}, & e = -\hat{\delta}, \\ \dot{f}_{\text{new}}(x, \hat{\alpha}, \hat{\delta}) = \hat{\alpha} \hat{\delta}^{\hat{\alpha}-1}, & e = \pm \hat{\delta}. \end{cases} \quad (27)$$

Then,

$$\begin{cases} \mathfrak{R}_1 \hat{\delta} + \mathfrak{R}_2 \hat{\delta}^2 + \mathfrak{R}_3 (1 - \cos \hat{\delta}) = \hat{\delta}^{\hat{\alpha}}, \\ -\mathfrak{R}_1 \hat{\delta} + \mathfrak{R}_2 \hat{\delta}^2 - \mathfrak{R}_3 (1 - \cos \hat{\delta}) = -\hat{\delta}^{\hat{\alpha}}, \\ \mathfrak{R}_1 + 2\mathfrak{R}_2 \hat{\delta} + \mathfrak{R}_3 \sin \hat{\delta} = \hat{\alpha} \hat{\delta}^{\hat{\alpha}-1}. \end{cases} \quad (28)$$

Sequentially, $\mathfrak{R}_1, \mathfrak{R}_2$, and \mathfrak{R}_3 can be determined as

$$\begin{cases} \mathfrak{R}_1 = \hat{\delta}^{\hat{\alpha}-1} \hat{\alpha} - \frac{(1-\hat{\alpha})\hat{\delta}^{\hat{\alpha}} \sin \hat{\delta}}{1 - \cos \hat{\delta} - \hat{\delta} \sin \hat{\delta}}, \\ \mathfrak{R}_2 = 0, \\ \mathfrak{R}_3 = \frac{(1-\hat{\alpha})\hat{\delta}^{\hat{\alpha}}}{1 - \cos \hat{\delta} - \hat{\delta} \sin \hat{\delta}}. \end{cases} \quad (29)$$

Thus, the expression of $f_{\text{new}}(\cdot)$ can be obtained as follows:

$$f_{\text{new}}(x, \hat{\alpha}, \hat{\delta}) = \begin{cases} |x|^{\hat{\alpha}} \text{sign}(x), & |x| > \hat{\delta}, \\ \left[\hat{\delta}^{\hat{\alpha}-1} \hat{\alpha} - \frac{(1-\hat{\alpha})\hat{\delta}^{\hat{\alpha}} \sin \hat{\delta}}{1 - \cos \hat{\delta} - \hat{\delta} \sin \hat{\delta}} \right] x + \frac{(1-\hat{\alpha})\hat{\delta}^{\hat{\alpha}}}{1 - \cos \hat{\delta} - \hat{\delta} \sin \hat{\delta}} (\text{ver sin}(|x|) \text{sign}(x)), & |x| \leq \hat{\delta}. \end{cases} \quad (30)$$

The corresponding function curves of the function $f_{\text{new}}(\cdot)$ are shown in Figure 3(b). Figure 3(b) shows that the

new nonlinear function $f_{\text{new}}(\cdot)$ exhibits better continuity and differentiability than the conventional function $\text{fal}(\cdot)$.

The nonlinear function $\text{fal}(\cdot)$ is actually an empirical knowledge of control engineering [34, 39]. However, it is nonderivable, and the high-frequency flutter phenomenon will be produced by the function $\text{fal}(\cdot)$. The new nonlinear function $f_{\text{new}}(\cdot)$ has the following characteristics: it is a continuous and derivable function which reduces the high-frequency flutter phenomenon, and the value of $\hat{\alpha}$ influences the nonlinearity degree of $f_{\text{new}}(\cdot)$; $f_{\text{new}}(\cdot)$ exhibits the characteristics of small errors ($|x| \leq \hat{\delta}$) with higher gains ($|f_{\text{new}}(x, \hat{\alpha}, \hat{\delta})| > |x|$); on the contrary, large errors ($|x| > \hat{\delta}$) correspond to lower gains ($|f_{\text{new}}(x, \hat{\alpha}, \hat{\delta})| < |x|$), so it can force the error signal to attenuate to zero quickly, it has the characteristic of fast convergence function, and the function has the characteristic of saturating the error. A FOPID has the weaknesses of being simple and tough, which may consequently make it more difficult to meet demands for the high quality of the control system [40]. As a result, an NFOPID sliding surface is designed, the error signal e passes through the nonlinear function $f_{\text{new}}(\cdot)$ to obtain $f_{\text{new}}(e(t))$, and the new nonlinear function $f_{\text{new}}(e(t))$ is applied on the integral and differential terms in the NFOPID sliding surface. Then, a novel NLSEF based on the new nonlinear function $f_{\text{new}}(e(t))$ compensates the insufficiency for relatively simple and rough signal processing of FOPID. The NFOPID sliding surface structure diagram is shown in Figure 4. Satisfactory comprehensive control performance in the sliding phase can be obtained by using the NFOPID manifold.

Definition 5. The proposed NFOPID sliding surface s_{NFOPID} can be defined as follows:

$$s_{\text{NFOPID}}(t) = K_p e(t) + K_i D_t^u (f_{\text{new}}(e(t), \hat{\alpha}, \hat{\delta})) + K_d D_t^\epsilon (f_{\text{new}}(e(t), \hat{\alpha}, \hat{\delta})), \quad (31)$$

where $K_p > 0$, $K_i > 0$, and $K_d > 0$.

We adopt the following reaching law:

$$\dot{s}_{\text{NFOPID}}(t) = -k s_{\text{NFOPID}}(t) - \eta \text{sign}(s_{\text{NFOPID}}(t)). \quad (32)$$

Taking the time derivative of the sliding mode surface (31), by Lemma 1, and substituting (31) into (32), we obtain

$$\begin{aligned} & K_p \dot{e}(t) + K_i D_t^{1+u} (f_{\text{new}}(e(t), \hat{\alpha}, \hat{\delta})) \\ & + K_d D_t^{\epsilon+1} (f_{\text{new}}(e(t), \hat{\alpha}, \hat{\delta})) \\ & = -k s_{\text{NFOPID}}(t) - \eta \text{sign}(s_{\text{NFOPID}}(t)). \end{aligned} \quad (33)$$

Sequentially, substituting (8) and (9) into (33), we obtain

$$\begin{aligned} & K_p \left(\dot{\omega}_r(t) - \frac{3p_n \varphi_f}{2J} i_q + \frac{T_L}{J} + \frac{B}{J} \omega(t) \right) \\ & + K_i D_t^{1+u} (f_{\text{new}}(e(t), \hat{\alpha}, \hat{\delta})) + K_d D_t^{1+\epsilon} (f_{\text{new}}(e(t), \hat{\alpha}, \hat{\delta})) \\ & = -k s_{\text{NFOPID}}(t) - \eta \text{sign}(s_{\text{NFOPID}}(t)). \end{aligned} \quad (34)$$

TABLE 1: Key parameters of the SMC-FOPID and SMC-NFOPID strategies.

Control strategy	K_i	K_p	K_d	u	ϵ	$\hat{\delta}$	$\hat{\alpha}$	k	η
SMC-FOPID	1	0.3	1	-0.01	0.01	N/A	N/A	20	15
SMC-NFOPID	1	0.3	1	-0.01	0.01	0.1	0.25	20	15

Then, on the basis of the proposed NFOPID sliding surface, the control law of the proposed SMC-NFOPID input can be obtained as follows:

$$\begin{aligned} i_q = & \frac{2J}{3p_n \varphi_f K_p} \left(\left(K_p \left(\dot{\omega}_r(t) + \frac{T_L}{J} + \frac{B}{J} \omega_r(t) \right) \right) \right. \\ & + K_p \left(k - \frac{B}{J} \right) e(t) + K_i D_t^{1+u} (f_{\text{new}}(e(t), \hat{\alpha}, \hat{\delta})) \\ & + K_d D_t^{1+\epsilon} (f_{\text{new}}(e(t), \hat{\alpha}, \hat{\delta})) + k K_i D_t^u (f_{\text{new}}(e(t), \hat{\alpha}, \hat{\delta})) \\ & \left. + k K_d D_t^\epsilon (f_{\text{new}}(e(t), \hat{\alpha}, \hat{\delta})) + \eta \text{sign}(s_{\text{NFOPID}}(t)) \right), \end{aligned} \quad (35)$$

where load torque T_L is regarded as external disturbances; however, in the case of the unknown load torque T_L , T_L is estimated by a novel second-order ESO (NSOESO) in this paper.

Expression of the traditional second-order ESO (TSOESO) is established as follows [34]:

$$\begin{cases} \bar{e} = Z_{21} - \omega, \\ \dot{Z}_{21} = Z_{22} - \tilde{\beta}_{01} \text{fal}(\bar{e}, \delta, \alpha) + \tilde{b}_0 i_q, \\ \dot{Z}_{22} = -\tilde{\beta}_{02} \text{fal}(\bar{e}, \delta, \alpha), \end{cases} \quad (36)$$

where ω is the mechanical rotor angular speed, $\tilde{\beta}_{01}$ and $\tilde{\beta}_{02}$ are the positive gain parameters of the TSOESO, and \tilde{b}_0 is an estimation of the compensation factor. Once the observer is designed and well tuned, Z_{21} is the observation value of ω and $\tilde{T}_L = -Z_{22} \tilde{b}_0$ is the estimated value of the load torque T_L . However, the nonlinear function $\text{fal}(\cdot)$ is nonderivable, and the high-frequency flutter phenomenon will be produced by the conventional nonlinear function. Therefore, an NSOESO is also designed on the basis of the new nonlinear function $f_{\text{new}}(\cdot)$. Expression of the NSOESO is established as follows:

$$\begin{cases} \bar{e} = Z_{21} - \omega, \\ \dot{Z}_{21} = Z_{22} - \beta_{01} f_{\text{new}}(\bar{e}, \hat{\delta}, \hat{\alpha}) + b_0 i_q, \\ \dot{Z}_{22} = -\beta_{02} f_{\text{new}}(\bar{e}, \hat{\delta}, \hat{\alpha}). \end{cases} \quad (37)$$

According to (8), (9), (32), and (37), (35) could then be expressed as follows:

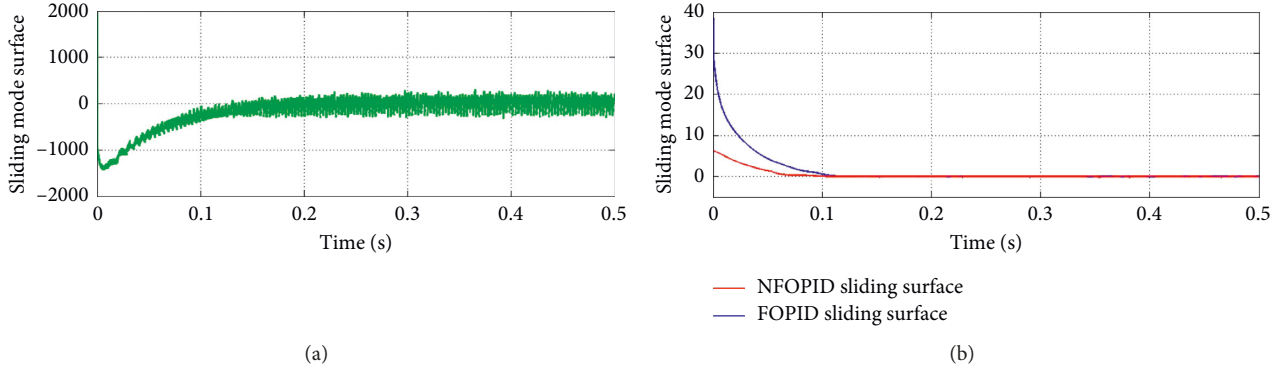


FIGURE 5: (a) Response curves of the traditional sliding surface. (b) Response curves of the FOPID sliding surface and the proposed NFOPID sliding surface.

$$\begin{aligned}
 i_q = & \frac{2J}{3p_n\varphi_f K_p} \left(\left(K_p \left(\dot{\omega}_r + \frac{\tilde{T}_L}{J} + \frac{B}{J} \omega_r \right) \right) \right. \\
 & + K_p \left(k - \frac{B}{J} \right) e(t) + K_i D_t^{1+u} (f_{\text{new}}(e(t), \hat{\delta}, \hat{\alpha})) \\
 & + K_d D_t^{1+\varepsilon} (f_{\text{new}}(e(t), \hat{\delta}, \hat{\alpha})) + k K_i D_t^u (f_{\text{new}}(e(t)) \hat{\delta}, \hat{\alpha})) \\
 & \left. + k K_d D_t^\varepsilon (f_{\text{new}}(e(t), \hat{\delta}, \hat{\alpha})) + \eta \text{sign}(s_{\text{NFOPID}}(t)) \right). \quad (38)
 \end{aligned}$$

4. Stability Analysis

The stability analysis is divided into two steps in this paper.

$$\begin{aligned}
 \dot{V} &= s_{\text{NFOPID}} \cdot \dot{s}_{\text{NFOPID}} \\
 &= s_{\text{NFOPID}} (K_p \dot{e}(t) + K_i D_t^{u+1} f_{\text{new}}(e(t)) + K_d D_t^{\varepsilon+1} f_{\text{new}}(e(t))) \\
 &= s_{\text{NFOPID}} (K_p (\dot{\omega}_r - bu + c(\tilde{T}_L + \Delta T_L) + a(\omega_r - e(t))) + K_i D_t^{u+1} f_{\text{new}}(e(t)) + K_d D_t^{\varepsilon+1} f_{\text{new}}(e(t))) \\
 &= s_{\text{NFOPID}} (K_p (\dot{\omega}_r - bu + a(\omega_r - e(t)) + K_i D_t^{u+1} f_{\text{new}}(\dot{e}(t)) + K_d D_t^{\varepsilon+1} f_{\text{new}}(e(t)) + K_p c(\tilde{T}_L + \Delta T_L))) \quad (40) \\
 &= s_{\text{NFOPID}} (-k s_{\text{NFOPID}} - \eta \text{sign}(s_{\text{NFOPID}}) + K_p c \Delta T_L) \\
 &= -k s_{\text{NFOPID}}^2 - \eta s_{\text{NFOPID}} \text{sign}(s_{\text{NFOPID}}) + K_p s_{\text{NFOPID}} c \Delta T_L \\
 &= -k s_{\text{NFOPID}}^2 - \eta |s_{\text{NFOPID}}| + K_p s_{\text{NFOPID}} c \Delta T_L.
 \end{aligned}$$

For notional brevity, we define $u = i_q$, $b = (3p_n\varphi_f)/(2J)$, $c = 1/J$, and $a = B/J$, where ΔT_L is the total disturbance of the system. The parameters of the SPMSM will change, but the variable is bounded. Thus, $c\Delta T_L < \lambda$, where λ is a constant, and it is an upper bound of $c\Delta T_L$. According to stability theory of Lyapunov function, if $\dot{V} < 0$ and $V > 0$ are satisfied, the closed-loop system is asymptotically stable, and then it can be obtained as follows:

Theorem 1. Consider the SPMSM system (8) and (9) with the load torque regarded as external disturbances (37) and under the SMC-NFOPID control law given by (38). Wherever the initial state, the control output can drive the initial state converge to the sliding manifold. Then, the tracking error can be bounded for a given reference mechanical rotor angular speed signal in finite time.

Proof.

Step 1. a Lyapunov function candidate of the proposed SMC-NFOPID is selected as

$$V = \frac{1}{2} s_{\text{NFOPID}}^2 > 0. \quad (39)$$

According to (8), (9), (31), and (32), the first-order time derivative (39) can be represented as follows:

$$-k s_{\text{NFOPID}}^2 - \eta |s_{\text{NFOPID}}| + K_p s_{\text{NFOPID}} c \Delta T_L < 0, \quad (41)$$

where $-k s_{\text{NFOPID}}^2 < 0$; consequently, if $\eta > K_p \lambda$ is satisfied, then $\dot{V} < 0$ is satisfied. Then, when time tends to reach infinity, $s_{\text{NFOPID}}(t)$ goes to zero. Accordingly, we can easily conclude that the sliding surface $s_{\text{NFOPID}}(t)$ will be bounded in finite time as $|s_{\text{NFOPID}}| \leq \Theta$.

Step 2. the stability and convergence property of the fractional order system have to be proved. It means that the

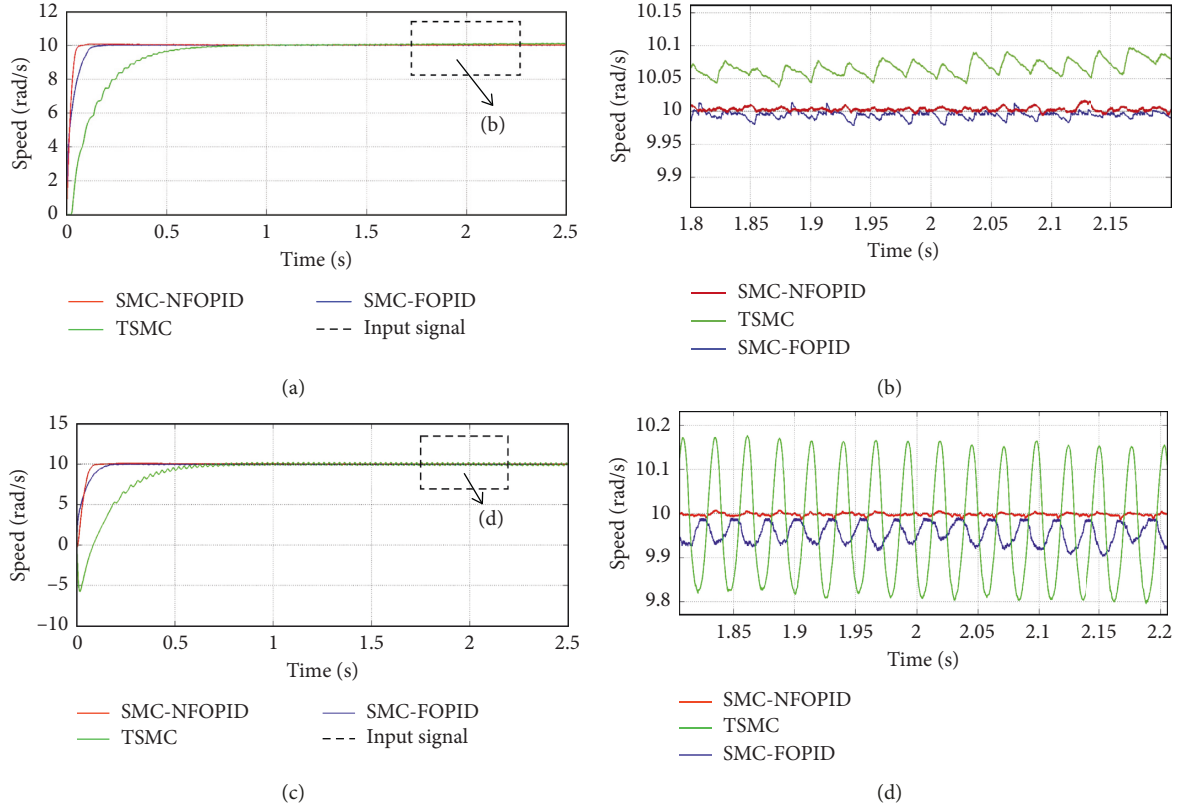


FIGURE 6: (a) Speed response curves in the absence of external load under three control strategies. (b) Partial enlarged view of speed response curves in the absence of external load. (c) Speed response curves with 5 N·m load under three control strategies. (d) Partial enlarged view of speed response curves with 5 N·m load.

finite-time convergence of the control error $e(t)$ will be briefly proved using the similar procedure from references [29, 41].

Combining $|s_{\text{NFOPID}}| \leq \Theta$ with equation (31), we obtain

$$\begin{cases} s_{\text{NFOPID}} = K_p e(t) + K_i D_t^u f_{\text{new}}(e(t)) + K_d D_t^\epsilon f_{\text{new}}(e(t)), \\ |s_{\text{NFOPID}}| \leq \Theta. \end{cases} \quad (42)$$

Using (42), the following form can be obtained:

$$\begin{aligned} e(t) + \frac{K_i}{K_p} D_t^u f_{\text{new}}(e(t)) \\ + \left(\frac{K_d}{K_p} - \frac{1}{K_p} s_{\text{NFOPID}} (D_t^\epsilon f_{\text{new}}(e(t)))^{-1} \right) D_t^\epsilon f_{\text{new}}(e(t)) = 0. \end{aligned} \quad (43)$$

When $K_d - s_{\text{NFOPID}} (D_t^\epsilon f_{\text{new}}(e(t)))^{-1} > 0$ holds, (43) will still remain in the NFOPID form as (31). According to (42) and (43), the system trajectory will persistently converge to the NFOPID sliding surface (31) until we have $|D_t^\epsilon f_{\text{new}}(e(t))| \leq (1/K_d)\Theta$.

Using (42), the following form can also be obtained:

$$\begin{aligned} e(t) + \left(\frac{K_i}{K_p} - \frac{1}{K_p} s_{\text{NFOPID}} (D_t^u f_{\text{new}}(e(t)))^{-1} \right) D_t^u f_{\text{new}}(e(t)) \\ + \frac{K_d}{K_p} D_t^\epsilon f_{\text{new}}(e(t)) = 0. \end{aligned} \quad (44)$$

Using the similar procedure to (44), we can also get $|D_t^u f_{\text{new}}(e(t))| \leq (1/K_i)\Theta$.

Sequentially, we have

$$\begin{aligned} |e(t)| &= \left| \frac{1}{K_p} s_{\text{NFOPID}} - \frac{K_i}{K_p} D_t^u f_{\text{new}}(e(t)) - \frac{K_d}{K_p} D_t^\epsilon f_{\text{new}}(e(t)) \right| \\ &\leq \left| \frac{1}{K_p} s_{\text{NFOPID}} \right| + \left| \frac{K_i}{K_p} D_t^u f_{\text{new}}(e(t)) \right| + \left| \frac{K_d}{K_p} D_t^\epsilon f_{\text{new}}(e(t)) \right| \leq \frac{3\Theta}{K_p}. \end{aligned} \quad (45)$$

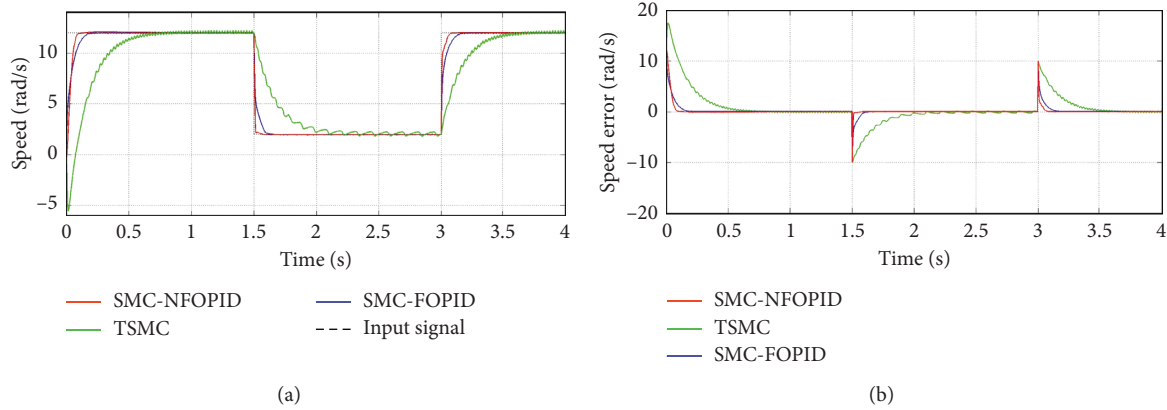


FIGURE 7: (a) Response curves under three control strategies for a square wave signal input. (b) Response error curves under three control strategies for a square wave signal input.

It means that the finite-time convergence of the control error $e(t)$ is briefly proved; then, the control error is bounded and the stability of the closed-loop control system is proved. This proves Theorem 1.

5. Comparative Simulations and Analysis

In order to validate the effectiveness of the proposed controller, we carry out the comparative simulations in the MATLAB/Simulink environment in this section.

The parameters of the simulation SPMSM are listed as follows: the nominal voltage $U = 400$ V, the stator phase resistance $R_s = 0.958 \Omega$, the cross-axis inductance $L_d = L_q = L = 5.25$ mH, the magnetic chain of permanent magnets $\varphi_f = 0.1827$ Wb, the moment of inertia $J = 0.009$ kg·m², the viscous damping $B = 0.008$ (Nm·s)/rad, and the pole pairs $p_n = 4$. The coefficient of the TSMC is designed as $c = 0.1$. Table 1 presents the parameters of the SMC-FOPID and the proposed SMC-NFOPID strategies.

To execute simulation, the reference speed is set as 10 rad/s at 0 s and the test time is set as 0.5 s. The sliding surfaces of three control strategies are shown in Figure 5. From Figure 5, it can be seen that the proposed SMC-NFOPID strategy reaches the sliding surface $s = 0$ in less time compared to the TSMC and SMC-FOPID strategies.

In the first simulation test, a comparison of step response is made, as shown in Figure 6. Figure 6(a) shows the reference speed is set as 10 rad/s at 0 s which is applied to the SPMSM in the absence of external load and test time is set as 2.5 s. It obviously shows that the proposed SMC-NFOPID strategy has a shorter adjustment time than those of the TSMC and SMC-FOPID strategies. Figure 6(c) shows the reference speed is set as 10 rad/s at 0 s which is applied to the SPMSM under the existence of 5 N·m load and the test time is set as 2.5 s. It evidently shows that the proposed SMC-NFOPID strategy also exhibits shorter response time than those of the TSMC and SMC-FOPID strategies. From Figure 6(b), it can be clearly seen that the TSMC and SMC-FOPID strategies have severe buffeting, and by comparison, the proposed SMC-NFOPID strategy is relatively smooth. Figure 6(d) shows that the proposed SMC-NFOPID strategy

still has a good tracking performance, and the tracking error is still small which is applied on the SPMSM with 5 N·m load; however, the TSMC and SMC-FOPID strategies become much worse.

Figures 7 and 8 show response curves under the TSMC, SMC-FOPID, and SMC-NFOPID strategies for a square wave signal input and a sinusoidal signal input, respectively. The results all show that the system with the SMC-NFOPID strategy has better tracking ability than those of the TSMC and SMC-FOPID strategies.

In order to display the influence of the nonderivable properties of the traditional function $\text{fal}(\cdot)$ compared with the new function $f_{\text{new}}(\cdot)$ on the effect of the control strategy, we do the following comparative simulation verifications. Figure 9 compares the time response curves of the NFOPID sliding surface based on the new function $f_{\text{new}}(\cdot)$ and the conventional function $\text{fal}(\cdot)$. We set the parameters of the conventional function the same as those of the new function $f_{\text{new}}(\cdot)$. The parameters of the conventional function $\text{fal}(\cdot)$ are designed as $\delta = 0.1$ and $\alpha = 0.25$. It can be seen obviously from Figure 9 that the NFOPID sliding surface based on the new function $f_{\text{new}}(\cdot)$ reduces the high-frequency flutter phenomenon significantly compared with the NFOPID sliding surface based on the traditional function $\text{fal}(\cdot)$. Figure 10 compares the estimation effect of the NSOESO and TSOESO, and we set the parameters of the TSOESO the same as those of the NSOESO. The parameters of the TSOESO are designed as $\tilde{\beta}_{01} = 2000$, $\tilde{\beta}_{02} = 150000$, $\tilde{b}_0 = 121$, $\tilde{\delta} = 0.1$, and $\tilde{\alpha} = 0.25$. The parameters of the NSOESO are designed as $\beta_{01} = 2000$, $\beta_{02} = 150000$, $b_0 = 121$, $\hat{\delta} = 0.1$, and $\hat{\alpha} = 0.25$. The reference speed is set as 10 rad/s at 0 s which is applied on the SPMSM, and the test time is set as 2.5 s. The response curves of the state variable Z_{21} with the TSOESO and NSOESO are shown in Figure 10, respectively. For well-turned ESO, Figure 10(a) shows that both the TSOESO and NSOESO can estimate the reference speed closely. However, it can be seen obviously from Figure 10(b) that the NSOESO exhibits better estimation ability than the TSOESO. As can be seen from Figures 9 and 10, because of the application of the new function $f_{\text{new}}(\cdot)$, the high-frequency flutter phenomenon is reduced significantly.

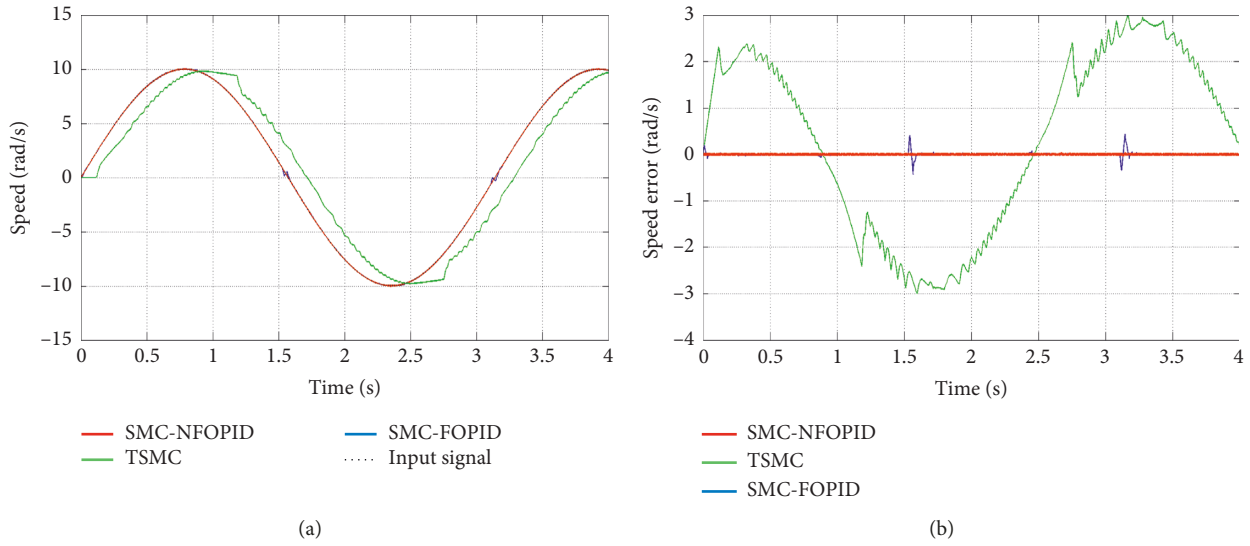


FIGURE 8: (a) Response curves under three control strategies for a sinusoidal signal input. (b) Response error curves under three control strategies for a sinusoidal signal input.

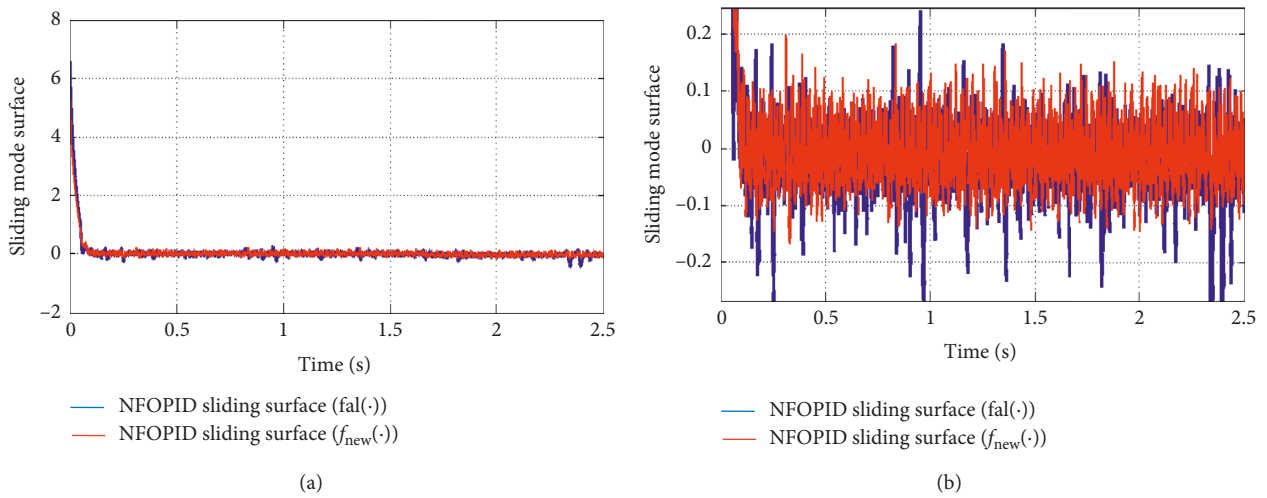


FIGURE 9: (a) Response curves of the NFOPID sliding surface based on the new function $f_{new}(\cdot)$ and the conventional function $f_{al}(\cdot)$. (b) Partial enlarged views of NFOPID sliding surface curves.

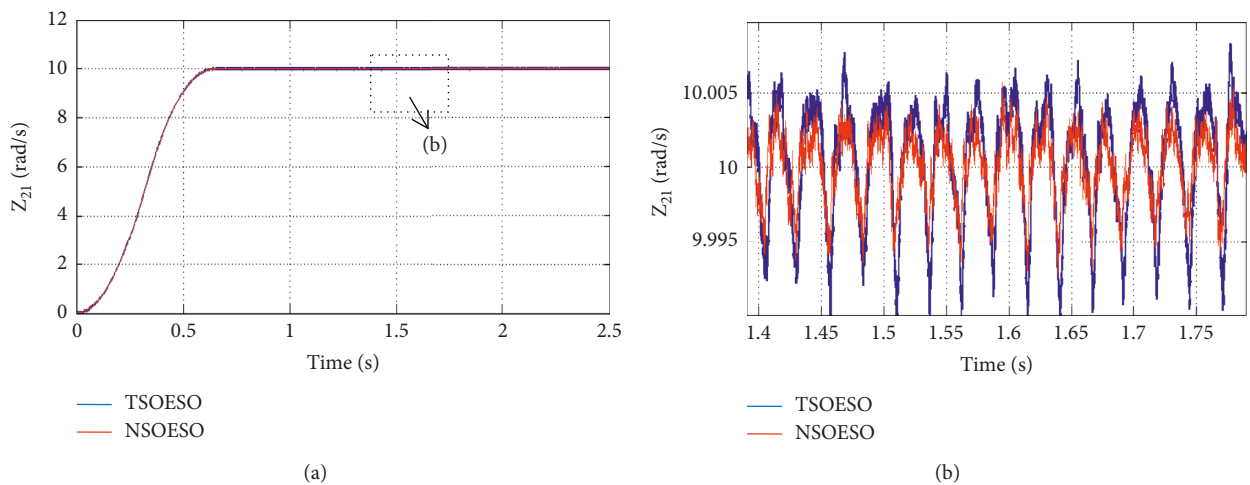


FIGURE 10: (a) Z_{21} curves under the TSOESO and NSOESO. (b) Partial enlarged views of Z_{21} curves.

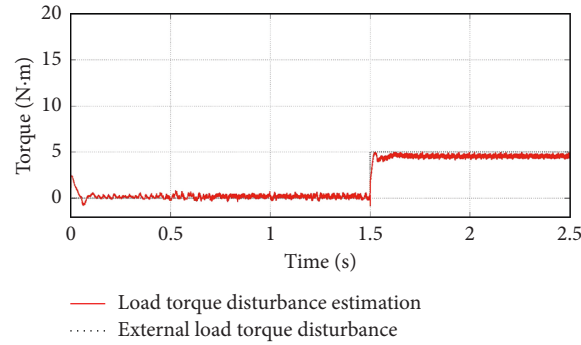


FIGURE 11: External load disturbance estimation under the NSOESO.

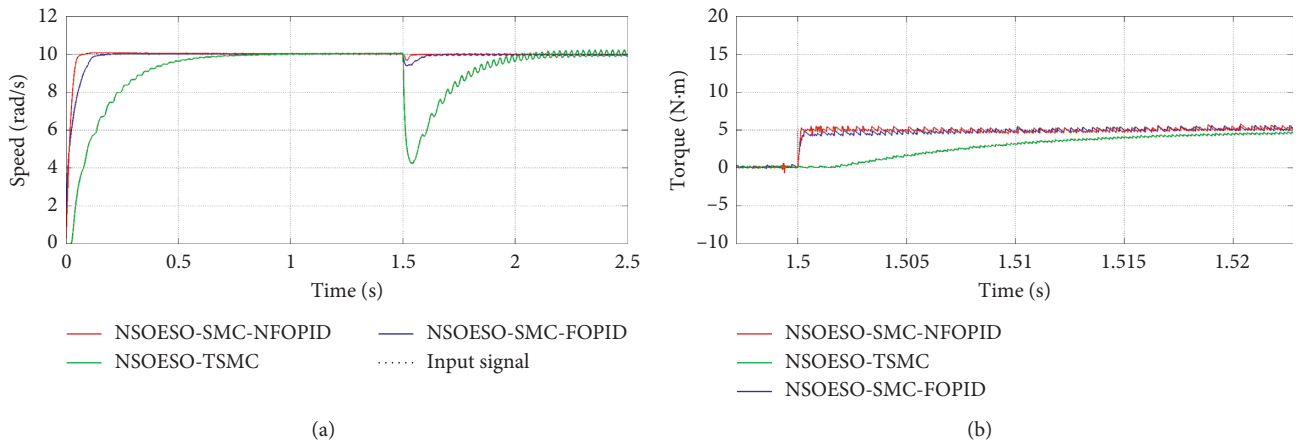


FIGURE 12: Response curves with an external load disturbance applied under three control strategies. (a) Speed response curves when load changes from 0 N·m to 5 N·m at 1.5 s. (b) Torque response curves when load changes from 0 N·m to 5 N·m at 1.5 s.

TABLE 2: Parameters of the overshoot amount and convergence time under three control strategies for an external load disturbance.

	NSOESO-TSMC			NSOESO-SMC-FOPID			NSOESO-SMC-NFOPID		
	Speed convergence time (s)	Speed overshoot amount (%)	Torque setting time (s)	Speed convergence time (s)	Speed overshoot amount (%)	Torque setting time (s)	Speed convergence time (s)	Speed overshoot amount (%)	Torque setting time (s)
Load changes from 0 N·m to 5 N·m	1.035	60.8	0.0282	0.128	6.5	0.0051	0.035	3.4	0.0002

In order to evaluate the performance of the proposed control strategy under an external disturbance, simulations are performed to verify the anti-interference ability of the proposed control strategy. As an external disturbance, the load torque T_L changes from 0 N·m to 5 N·m at 1.5 s. Figure 11 shows the result that the NSOESO estimates the load torque disturbance T_L . A comparison of control performance is given when the external load disturbance is applied on the motor under three control strategies in Figure 12 and Table 2.

Figure 12 and Table 2 show the dynamic responses of the speed and torque when the external load changes from 0 N·m to 5 N·m at 1.5 s. The speed convergence time of the SMC-NFOPID strategy with the NSOESO (NSOESO-SMC-

NFOPID) is 0.035 s shorter than those of the TSMC strategy with the NSOESO (NSOESO-TSMC) and the SMC-FOPID strategy with the NSOESO (NSOESO-SMC-FOPID). Figure 12 and Table 2 also show that the overshoot amount of the proposed control strategy is 3.4% lower than those of the NSOESO-TSMC and NSOESO-SMC-FOPID strategies, and the torque response time of the proposed control strategy is 0.0002 s shorter than those of the NSOESO-TSMC and NSOESO-SMC-FOPID strategies.

According to the above simulation results, it is obvious that the proposed control strategy exhibits shorter convergence time and smaller overshoot amount than those of the conventional control strategies, so the control effect of the proposed control strategy has been verified.

6. Conclusions

This paper presents a novel SMC strategy composed of the SMC-NFOPID and the NSOESO for the speed operation of the SPMSM. First, a novel NLSEF is designed on the basis of a new continuous and derivable nonlinear function; then, an SMC-NFOPID is designed on the basis of the FOPID sliding surface with the combination of the novel NLSEF. Furthermore, an NSOESO based on the new nonlinear function is designed. As a consequence, a novel compound control strategy with the SMC-NFOPID based on the NSOESO for the speed operation of the SPMSM is presented in this paper. The stability of the proposed compound controller is proved via the Lyapunov stability theorem. In order to validate the effectiveness of the proposed controller, we carry out the comparative simulations in the MATLAB/Simulink environment. The simulation results confirm that the proposed SMC-NFOPID strategy reaches the sliding surface in less time compared with the TSMC and SMC-FOPID strategies, and the simulation results for the SPMSM are given to show that the proposed composite controller exhibits better dynamic performance, static performance, and robustness against external disturbances than the conventional SMC and SMC-FOPID strategies.

In the future, an adaptive law will be constructed to design switching feedback law gains for the SMC-NFOPID strategy.

Data Availability

The data used to support the findings of this study are available from the corresponding author upon request.

Conflicts of Interest

The authors declare that there are no conflicts of interest regarding the publication of this paper.

Acknowledgments

This work was supported by the National Natural Science Foundation of China under Grant no. 61703202 and by the Key Research Development Project of Jiangsu Province under Grant BE no. 2017164.

References

- [1] B.-Y. Liu, C.-A. Zhu, and X.-Z. Guo, "Current-loop control for the pitching axis of aerial cameras via an improved ADRC," *Mathematical Problems in Engineering*, vol. 2017, Article ID 6162194, 8 pages, 2017.
- [2] G. Mohammad and L. Saeed, "Control of flywheel energy storage systems in the presence of uncertainties," *IEEE Transactions on Sustainable Energy*, vol. 10, no. 1, pp. 36–45, 2019.
- [3] E. Lu, W. Li, X. Yang, and Y. Liu, "Anti-disturbance speed control of low-speed high-torque PMSM based on second-order non-singular terminal sliding mode load observer," *ISA Transactions*, vol. 88, pp. 142–152, 2019.
- [4] S. Li and Z. Liu, "Adaptive speed control for permanent-magnet synchronous motor system with variations of load inertia," *IEEE Transactions on Industrial Electronics*, vol. 56, no. 8, pp. 3050–3059, 2009.
- [5] J. Yu, P. Shi, and L. Zhao, "Finite-time command filtered backstepping control for a class of nonlinear systems," *Automatica*, vol. 92, pp. 173–180, 2018.
- [6] J.-D. Yan, H. Wang, S.-D. Huang, and Y.-H. Lan, "Disturbance observer-based backstepping control of PMSM for the mine traction electric locomotive," *Mathematical Problems in Engineering*, vol. 2018, Article ID 7253210, 10 pages, 2018.
- [7] X.-D. Liu, K. Li, and C.-H. Zhang, "Improved backstepping control with nonlinear disturbance observer for the speed control of permanent magnet synchronous motor," *Journal of Electrical Engineering & Technology*, vol. 14, no. 1, pp. 275–285, 2019.
- [8] X. Zhang, B. Hou, and Y. Mei, "Deadbeat predictive current control of permanent-magnet synchronous motors with stator current and disturbance observer," *IEEE Transactions on Power Electronics*, vol. 32, no. 5, pp. 3818–3834, 2017.
- [9] M. Siami, D. A. Khaburi, A. Abbaszadeh, and J. Rodriguez, "Robustness improvement of predictive current control using prediction error correction for permanent-magnet synchronous machines," *IEEE Transactions on Industrial Electronics*, vol. 63, no. 6, pp. 3458–3466, 2016.
- [10] Y. Zuo, X. Zhu, L. Quan, C. Zhang, Y. Du, and Z. Xiang, "Active disturbance rejection controller for speed control of electrical drives using phase-locking loop observer," *IEEE Transactions on Industrial Electronics*, vol. 66, no. 3, pp. 1748–1759, 2019.
- [11] G. Wang, R. Liu, N. Zhao, D. Ding, and D. Xu, "Enhanced linear ADRC strategy for HF pulse voltage signal injection-based sensorless IPMSM drives," *IEEE Transactions on Power Electronics*, vol. 34, no. 1, pp. 514–525, 2019.
- [12] H. Chaoui and P. Sicard, "Adaptive fuzzy logic control of permanent magnet synchronous machines with nonlinear friction," *IEEE Transactions on Industrial Electronics*, vol. 59, no. 2, pp. 1123–1133, 2012.
- [13] F.-J. Lin, Y.-C. Hung, J.-C. Hwang, and M.-T. Tsai, "Fault-tolerant control of a six-phase motor drive system using a Takagi-Sugeno-Kang type fuzzy neural network with asymmetric membership function," *IEEE Transactions on Power Electronics*, vol. 28, no. 7, pp. 3557–3572, 2013.
- [14] C. Mu and H. He, "Dynamic behavior of terminal sliding mode control," *IEEE Transactions on Industrial Electronics*, vol. 65, no. 4, pp. 3480–3490, 2018.
- [15] Z. Ma and G. Sun, "Dual terminal sliding mode control design for rigid robotic manipulator," *Journal of the Franklin Institute*, vol. 355, no. 18, pp. 9127–9149, 2018.
- [16] D.-X. Zhang, Y.-W. Fang, P.-F. Yang, Y.-L. Wu, and T.-X. Liu, "A new control method for second-order multiple models control system based on global sliding mode," *Mathematical Problems in Engineering*, vol. 2018, Article ID 5709162, 8 pages, 2018.
- [17] C. Mu, W. Xu, and C. Sun, "On switching manifold design for terminal sliding mode control," *Journal of the Franklin Institute*, vol. 353, no. 7, pp. 1553–1572, 2016.
- [18] Q. Wang, H. Yu, M. Wang, and X. Qi, "An improved sliding mode control using disturbance torque observer for permanent magnet synchronous motor," *IEEE Access*, vol. 7, pp. 36691–36701, 2019.
- [19] S. Li, M. Zhou, and X. Yu, "Design and implementation of terminal sliding mode control method for PMSM speed regulation system," *IEEE Transactions on Industrial Informatics*, vol. 9, no. 4, pp. 1879–1891, 2013.

- [20] W. Xu, Y.-J. Jiang, and C.-X. Mu, "Novel composite sliding mode control for PMSM drive system based on disturbance observer," *IEEE Transactions on Applied Superconductivity*, vol. 26, no. 7, pp. 1–5, 2016.
- [21] P.-P. Xia, Y.-T. Deng, Z.-Q. Wang, and H.-W. Li, "Speed adaptive sliding mode control with an extended state observer for permanent magnet synchronous motor," *Mathematical Problems in Engineering*, vol. 2018, Article ID 6405923, 13 pages, 2018.
- [22] Y. Deng, J. Wang, H. Li, J. Liu, and D. Tian, "Adaptive sliding mode current control with sliding mode disturbance observer for PMSM drives," *ISA Transactions*, vol. 88, pp. 113–126, 2019.
- [23] A. Wang, X. Jia, and S. Dong, "A new exponential reaching law of sliding mode control to improve performance of permanent magnet synchronous motor," *IEEE Transactions on Magnetics*, vol. 49, no. 5, pp. 2409–2412, 2013.
- [24] Y. Tang, X. Zhang, D. Zhang, G. Zhao, and X. Guan, "Fractional order sliding mode controller design for antilock braking systems," *Neurocomputing*, vol. 111, pp. 122–130, 2013.
- [25] B. Zhang, Y. Pi, and Y. Luo, "Fractional order sliding-mode control based on parameters auto-tuning for velocity control of permanent magnet synchronous motor," *ISA Transactions*, vol. 51, no. 5, pp. 649–656, 2012.
- [26] C. Yin, X. Huang, Y. Chen, S. Dadras, S.-M. Zhong, and Y. Cheng, "Fractional-order exponential switching technique to enhance sliding mode control," *Applied Mathematical Modelling*, vol. 44, pp. 705–726, 2017.
- [27] N.-N. Yang, C.-J. Wu, R. Jia, and C.-X. Liu, "Fractional-order terminal sliding-mode control for buck DC/DC converter," *Mathematical Problems in Engineering*, vol. 2016, Article ID 6935081, 7 pages, 2016.
- [28] K. D. E. Kerrouche, L. Wang, A. Mezouar, L. Boumediene, and A. Van Den Bossche, "Fractional-order sliding mode control for D-STATCOM connected wind farm based DFIG under voltage unbalanced," *Arabian Journal for Science and Engineering*, vol. 44, no. 3, pp. 2265–2280, 2019.
- [29] Y. Wang, J. Chen, F. Yan, K. Zhu, and B. Chen, "Adaptive super-twisting fractional-order nonsingular terminal sliding mode control of cable-driven manipulators," *ISA Transactions*, vol. 86, pp. 163–180, 2019.
- [30] N. Z. Davijani, G. Jahanfarnia, and A. E. Abharian, "Nonlinear fractional sliding mode controller based on reduced order FNP model for output power control of nuclear research reactors," *IEEE Transactions on Nuclear Science*, vol. 64, no. 1, pp. 713–723, 2017.
- [31] Q. Gao, Y. Hou, J. Liu et al., "An extended state observer based fractional order sliding-mode control for a novel electro-hydraulic servo system with ISO-actuation balancing and positioning," *Asian Journal of Control*, vol. 21, no. 1, pp. 289–301, 2019.
- [32] E. Govinda Kumar and J. Arunshankar, "Control of nonlinear two-tank hybrid system using sliding mode controller with fractional-order PI-D sliding surface," *Computers & Electrical Engineering*, vol. 71, pp. 953–965, 2018.
- [33] X. Rui, W. Yin, Y. Dong, L. Lin, and X. Wu, "Fractional-order sliding mode control for hybrid drive wind power generation system with disturbances in the grid," *Wind Energy*, vol. 22, no. 1, pp. 49–64, 2019.
- [34] J. Han, "From PID to active disturbance rejection control," *IEEE Transactions on Industrial Electronics*, vol. 56, no. 3, pp. 900–906, 2009.
- [35] Q. Li, J. Yuan, and B. Zhang, "Extended state observer based output control for spacecraft rendezvous and docking with actuator saturation," *ISA Transactions*, vol. 88, pp. 37–49, 2019.
- [36] C. Hua, J. Li, Y. Yang, and X. Guan, "Extended-state-observer-based finite-time synchronization control design of teleoperation with experimental validation," *Nonlinear Dynamics*, vol. 85, no. 1, pp. 317–331, 2016.
- [37] W. Xu, R. Dian, Y. Liu, D. Hu, and J. Zhu, "Robust flux estimation method for linear induction motors based on improved extended state observers," *IEEE Transactions on Power Electronics*, vol. 34, no. 5, pp. 4628–4640, 2019.
- [38] C.-K. Lai and K.-K. Shyu, "A novel motor drive design for incremental motion system via sliding-mode control method," *IEEE Transactions on Industrial Electronics*, vol. 52, no. 2, pp. 499–507, 2005.
- [39] Z.-Q. Gao, Y. Huang, and J.-Q. Han, "An alternative paradigm for control system design," in *Proceedings of the 40th IEEE Conference on Control and Decision*, pp. 4578–4585, Orlando, FL, USA, December 2001.
- [40] J. Song, L. Wang, G. Cai, and X. Qi, "Nonlinear fractional order proportion-integral-derivative active disturbance rejection control method design for hypersonic vehicle attitude control," *Acta Astronautica*, vol. 111, pp. 160–169, 2015.
- [41] Y. Wang, S. Jiang, B. Chen, and H. Wu, "A new continuous fractional-order nonsingular terminal sliding mode control for cable-driven manipulators," *Advances in Engineering Software*, vol. 119, pp. 21–29, 2018.



Hindawi

Submit your manuscripts at
www.hindawi.com

